A Letters Journal Exploring the Frontiers of Physics

December 2019

EPL, **128** (2019) 58001 www.epljournal.org
doi: 10.1209/0295-5075/128/58001

Amorphous titanium-oxide supercapacitors with high capacitance

Mikio Fukuhara[1(a)], Tomoyuki Kuroda[1], Fumihiko Hasegawa[1], Yasuyuki Shirai[1], Tomoyuki Suwa[1], Toshiyuki Hashida[2] and Masahiko Nishijima[3]

[1] *New Industry Creation Hatchery Center, Tohoku University - Sendai 980-8579, Japan*
[2] *Fracture and Reliability Research Institute, Graduate School of Engineering, Tohoku University Sendai 980-8579, Japan*
[3] *The Electron Microscopy Center, Tohoku University - Aoba, Sendai 980-8577, Japan*

received 9 May 2019; accepted in final form 19 December 2019
published online 4 February 2020

PACS 84.32.Tt – Capacitors
PACS 78.55.Qr – Amorphous materials; glasses and other disordered solids
PACS 61.46.-w – Structure of nanoscale materials

Abstract – An amorphous titanium-oxide film oxidized anodically on amorphous Ti–10at%V–15at%Si alloy ribbons demonstrated excellent electric properties. Specifically, it showed a remarkable increase in parallel capacitance *Cp*, series capacitance *Cs*, time constant *RCs*, and decrease in the dielectric loss with decreasing frequency. The oblate semicircle after a semicircle with a Warburg region in the Nyquist diagram and rapid increases in the real impedance in the low-frequency region in the Bode diagram demonstrated a parallel circuit comprising an electric transport resistance *Re* (0.64 MΩ), and a high electric double-layer capacitance C_{dl} (604.0 μF/cm^2) at a nanometer-sized (∼53 nm in convex size) uneven surface between an upper $(Ti_{0.84}V_{0.11}Si_{0.05})O_{1.655}$ layer approximately 45-nm deep and air. The superior capacitances could be elucidated by electrostatic induction of a large positive charge to the uneven oxide surface based on the electronic conduction state derived from TiO_2/VO_2 nanostructural interfaces in the upper oxide layer.

Introduction. – Since the 1990s, a significant amount of scientific and technological research has been reported on the storage of electrical energy [1–6]. Over the past three decades, chemical and material researchers have focused on power-source devices such as batteries and fuel cells. In addition to the above, the most well-known electrochemical capacitor is the electric double-layer capacitor (EDLC) in which the interfaces of high-specific-area materials such as porous carbon materials and porous metal oxides are charged and discharged by ion or radical diffusion [3,5,6]. Generally, a dc battery and an ac capacitor operate differently to provide practical use of electric storage. The ability to store charge for both dc and ac applications would require significant advancements in electronic devices and electric power applications. Recently, we determined that amorphous titanium-oxides (ATOs) and aluminum-oxides (AAOs), exhibiting an *RC* constant larger than that of an EDLC [7] and a switching effect of positive and negative electricity from the atmosphere [8,9], respectively, could be regarded as dc/ac converting devices with nanometer-sized uneven surfaces [10,11].

Expecting high capacitances, we reported a Ti–Ni–Si amorphous alloy supercapacitor [9], constructed using a distributed constant-equipment circuit with a high resistance and low capacitance. This was built using an amorphous TiO_{2-x} surface containing numerous 50–70 nm cavities with a high work function of 5.5 eV [9,12], which could illuminate a red LED for 37 ms after being charged with 1 mA at 10 V [9,10]. These materials store ac electricity from 193 to 453 K with a voltage variation between 10 and 150 V and a dc capacitance of ∼4.8 F (∼52.8 kF/cm^3). A typical requirement for electric storage is a surface with nanometer-sized cavities and high electrical resistance. The amorphous materials of interest are completely different from the materials of the conventional "wet" cells, such as EDLCs and secondary cells, which are controlled by ion diffusivity. We termed this device a "dry" electric-distributed constant capacitor (EDCC) [7–12]. In this study, Ti–V–Si alloys were chosen as starting alloys for the formation of passive oxide films with nanometer-sized uneven structures using a valve metal of vanadium to

(a) E-mail: fukuhara@niche.tohoku.ac.jp

achieve a larger capacitance compared to those attained with Ti–Ni–Si alloys [7–10,12].

Experiments. – Ti–10at%V–15at%Si alloy ingots (compositions provided in nominal atomic percentage) were prepared by arc-melting the mixtures of Ti (99.95% purity), Si (99.999% purity), and V (99.9% purity) in an argon atmosphere purified by Ti-gettering. 50 μm thick and 1 mm wide ribbon specimens were prepared from the ingots by the rapid solidification of the melt on a single copper roller in He atmosphere at a tangential velocity of 52.3 m/s, using a single-wheel melt-quenching apparatus (NEV-A05-R10S, Nisshin Giken).

The subsequent anodic oxidation of the specimens was performed for 3.6 ks in 0.4 M H_2SO_4 at 60 V and 278 K. The sample structure of the anodic oxidized specimens was examined at 40 kV by X-ray diffraction (XRD) in the reflection mode with monochromatic Cu Kα radiation. The surface morphologies were analyzed via atomic force microscopy (AFM: SPA400 SII Nano Technology) using the tapping scan mode for a scanning window of $0.5 \times 0.5\ \mu m^2$ with $512^x \times 256^y$ measurement points.

The transmission electron microscopy (TEM) specimens were prepared by a focused ion beam (FIB; Quanta 3D Dual Beam system, Thermo Fisher Scientific)) using the lift-out method. Following this, the depths of layers were determined from the elemental mapping of Ti, V, Si, and O by scanning transmission electron microscopy (STEM) with an aberration-corrected TEM (Titan^3 G2 60-300 Probe Corrector, Thermo Fisher Scientific) at 200 kV. The depth profile of the elements was carried out by scanning XPS microprobe (Thermo Fisher Scientific, Theta Probe).

A silver coat of 0.5 mm in diameter was applied on a specimen (1 mm wide, 40 μm thick, and 10 mm long) with double-oxidized surfaces to prevent the contact problem. Subsequently, the specimen was directly sandwiched between two copper ribbons beneath two pieces of glass plates using a clamp. The capacitance of the specimen was measured using galvanostatic charge/discharge by a potentiostat/galvanostat (SP-150, BioLogic Science) at frequencies between 1 mHz and 1 MHz under a constant voltage of 10 mV at 278 K. All the electronic measurements were performed in an Al shield box to prevent the generation of electromagnetic fields in the environment.

Results and discussion. – Because a small amount of Ni remains in the amorphous oxide layer that is anodically oxidized on Ti–Ni–Si amorphous alloys [12], we used amorphous Ti–V–Si alloys to form rigid passive oxide films for this study. Because the electric capacitance of ATOs increases proportionally to the negative sixth power of the convex diameter, d up to 7 mF/cm^2 [9,10], we used the anodic polarization method to form a nanometer-sized uneven surface. The current time curves of the Ti–15at%Ni–15at%Si and Ti–10at%V–15at%Si amorphous alloys anodically oxidized at 60 and 50 V, respectively, are shown in fig. 1(a). Although both the curves are

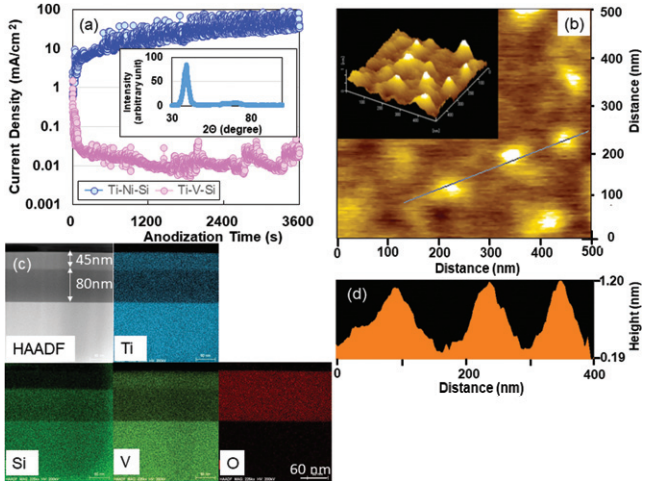

Fig. 1: Current time curves of the Ti–Ni–Si and Ti–V–Si alloys during anodization at 50 and 60 V for 3,600 s in 0.4 M H_2SO_4, respectively. (b) AFM image and (d) heights measured from the valley bottom along the blue line, and (c) HAADF-STEM image and mapping profiles of Ti, Si, V, and O for the anodically oxidized Ti–V–Si alloy. Inset: (a) X-ray pattern for the anodized specimen of the Ti–V–Si amorphous alloy ribbon.

characterized by continuous spark-discharging behaviors for the formation of uneven oxide surfaces [13,14], the latter curve stabilizes at 0.01 mA/cm^2, whereas the former curve increases gradually with the anodization time. This clearly demonstrates the passivation of the oxide film in the latter by the usage of the valve metal, V. The XRD pattern (fig. 1(a), inset) can be regarded to be similar to those of a Ti-based amorphous alloy coated with amorphous titanium-oxide layers and anodically oxidized Ti–15at%Ni–15at%Si alloys [7]. The primary broad peak ($\sim$39° in 2θ) is different from those ($\sim$29° and $\sim$24° in 2θ) of amorphous vanadium [15] and silicon [16] oxides. Figure 1(b) shows a three-dimensional AFM topography image of the surface structure of the anodically oxidized Ti–V–Si amorphous specimen, exhibiting an uneven convex surface of $\sim$53 nm. The uneven surface is also observed for the Ti–Ni–Si [13]. However, the depth ($\sim$1 nm) of the sunken location of the former is shallower than that ($\sim$82 nm) of the latter. In the high-angle annular dark-field scanning TEM (HAADF-STEM) images and elemental mapping of Ti, V, Si, and O in fig. 1(c), we observe two layers; the upper $(Ti_{0.84}V_{0.11}Si_{0.05})O_{1.655}$ oxide of depth 45 nm and lower $(Ti_{0.60}V_{0.12}Si_{0.28})\ O_{1.52}$ oxide of depth 80 nm on the Ti–V–Si alloy. The formation of the lower oxide layer with a larger formation energy (−908.5 kJ/mol [17]) of SiO_2 could be prior to that of the upper one having a smaller formation energy (−718.0 kJ/mol [18]) of VO_2. Particularly, the metallic compositions, $Ti_{0.84}V_{0.11}Si_{0.05}$ and $Ti_{0.60}V_{0.12}Si_{0.27}$ of the upper and lower layers, respectively, suggest a phase separation of metallic glass $Ti_{0.72}V_{0.115}Si_{0.165}$ which corresponds to a stability region of the amorphous phase in the Ti–V–Si system [19]. The nanoscale phase separation

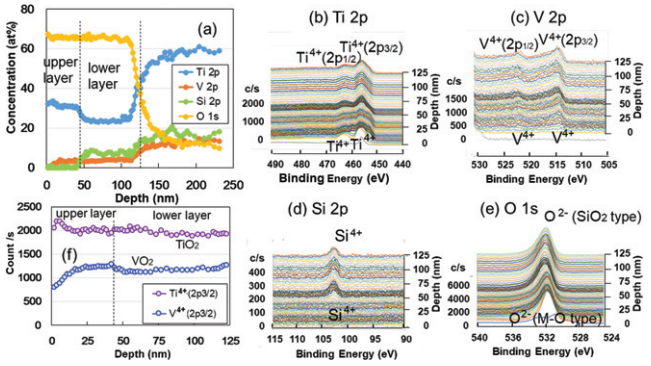

Fig. 2: Depth concentration profile (a) of Ti, V, Si and O and three-dimensional Ti $2p$ (b), V $2p$ (c), Si $2p$ (d) and O $1s$ (e) spectra and TiO_2 and VO_2 variation (f) in upper and lower oxide layers of anodic oxidized specimen.

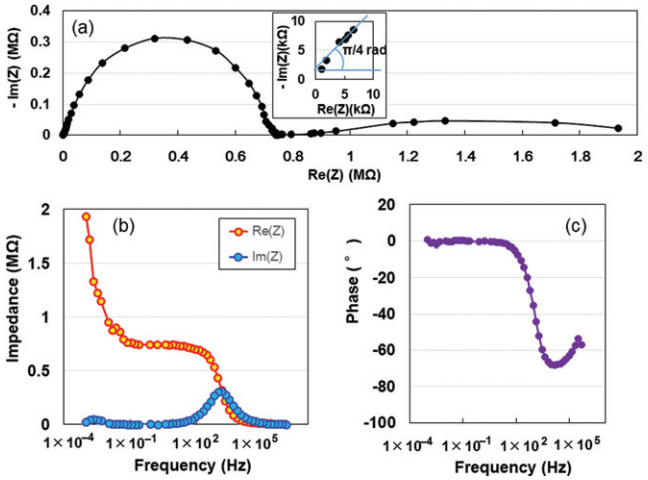

Fig. 3: Nyquist plot as a function of the frequency for the ATO device (a). Bode plots as a function of the frequency for the real and imaginary impedances (b) and phase angle (c).

could be derived from the spinodal decomposition mechanism [20] in the anodic polarization occurring at room temperature. In comparison with the thickness of the anodically oxidized films for the Ti–Ni–Si [21] and Al–Y [22] amorphous alloys, that (45 nm) of the upper layer is thinner than 200 nm and 15 μm for ATOs and AAOs, respectively, owing to the use of the valve metal. The upper layer would be a rigid passive amorphous oxide.

The depth profile of Ti, Si, V and O elements is shown in fig. 2(a). The depth dependence of these concentration files reveals two oxide layers (∼45 and ∼80 nm deep) on the Ti–V–Si alloy. Three-dimensional profiles of Ti $2p$ (fig. 2(b)), V $2p$ (fig. 2(c)), Si $2p$ (fig. 2(d)) and O $1s$ (fig. 2(e)) spectra identify two compositions of TiO_2 and VO_2 in the upper layer and three compositions of TiO_2, SiO_2 and VO_2 in the lower layer [23]. Both TiO_2 and VO_2 phases exist uniformly in the oxide layers at the inside of 20 nm (fig. 2(f)). The specimen was golden.

To analyze the electrostatic contribution of the specimen nondestructively, we measured twice the ac impedance from 1 mHz to 1 MHz using the Nyquist and Bode diagrams at room temperature. The repeated results were almost the same. A complex-plane (Nyquist) plot of the impedance data is shown in fig. 3(a). The impedance variation of the alloy with frequency follows the combined pattern of a line slope of $\pi/4$ rad and two semicircles, an almost semitrue circle with a lower resistance, and an oblate circle with a higher resistance. The $\pi/4$ rad region (Warburg regions) is a consequence of the distributed resistance/capacitance in porous electrode [24,25]. This suggests that the electrode is an ATO film with a porous surface with a high resistance. A reactance, R, of 0.64 (1.36–0.74) MΩ and relaxation time, RC_{total}, of 75.73 s at the top of the oblate semicircle are derived from the formula: $RC_{total} = 1/(2\pi f_{max})$, where f_{max} (=2.1 mHz) is the peak frequency. Thus, the total capacitance of the specimen, C_{total}, is calculated to be 54.93 μF (604.0 μF/cm^2). This value is 24 times larger than that (∼25 μF/cm^2) [26] of a conventional supercapacitor. If the R and specific surfaces of the ATO increase, the C_{total} of the ATO will increase still further. Figure 3(b) shows the frequency dependence of the real and imaginary impedances. A rapid increase is shown in the real impedance compared with the imaginary impedance in the low-frequency region. Moreover, the capacitive behavior (near 0 rad phase angle) in the frequency region between 100 and 0.001 Hz (fig. 3(c)) is a clear evidence of a parallel-RC circuit. Thus, the ATO films with a nanometer-sized uneven surface between the $(Ti_{0.84}V_{0.11}Si_{0.05})O_{1.655}$ oxide and air offer an electric distributed constant structure for enhancing the electric capacitance. Furthermore, because the shallow valleys, as shown in fig. 1(d), improve the charging/discharging characteristics at high frequencies [27], it will not be desirable for solid-state supercapacitors to exhibit a high–aspect-ratio nanotube structure on the ATO [7]. An ATO with a nanometer-sized uneven surface could not be realized using crystalline titanium-based alloys, but could be realized using amorphous alloys [28]. On the other hand, the discharging behavior of the ATO under constant current of 1 nA after prompt charging up to 10 V at the dc current of 1 mA is 1/1000 shorter than that of AAO [8,9], independent of V and Ni. Thus the ATO demonstrates inferior characteristics for dc electric storage, but superior capacitance in the low-frequency region.

We can store ac electricity using a rectifier. The series and parallel capacitances and RCs and RCp time constants at an applied voltage of 10 V at room temperature are presented in fig. 4(a) as a function of frequency. Both the capacitances increase exponentially with decreasing frequency. The total capacitance C_{total}, 54.93 μF (604.0 μF/cm^2) at the top (1.378 MΩ, 2.1 mHz) of the oblate semicircle in fig. 3(a) is approximately 0.045 and 125.8 times the Cs and Cp at 2.1 mHz in fig. 4(a), respectively. This difference suggests a combined parallel-series circuit for the specimen used in this study.

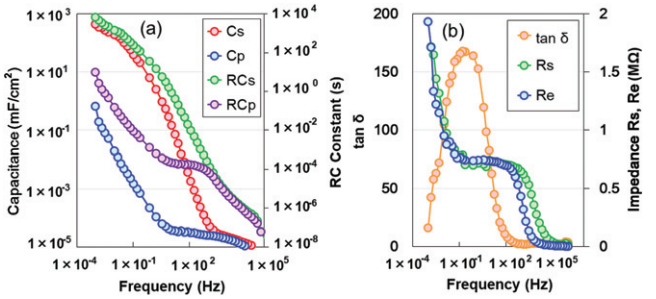

Fig. 4: Frequency dependence of the series and parallel capacitances, *RC* time constant for *RCs* and *RCp* (a) and electric loss, tan δ, and series *Rs* and parallel *Re* resistances (b).

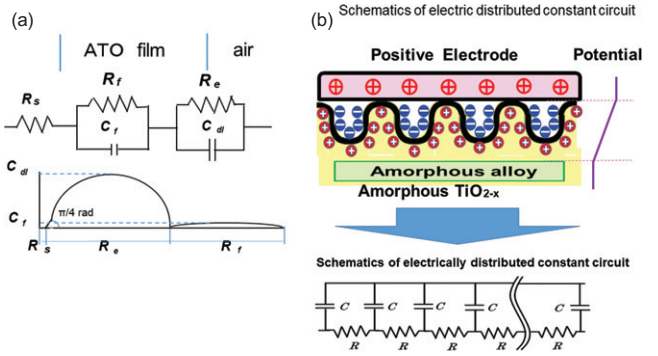

Fig. 5: Equivalent circuit (a) corresponding to the Nyquist diagram in fig. 3(a). (b) Schematic of the fabricated ATO device with an electric-distributed constant equipment circuit forming the amorphous $(Ti_{0.84}V_{0.11}Si_{0.05})O_{1.655}$ surface.

The *RCs* increases parabolically in the entire frequency range with decreasing frequency. Contrastingly, *RCp* increases parabolically from 1 MHz to 1 kHz, saturates from 1 kHz to 10Hz, and subsequently again parabolically increases up to approximately 10 s. The 3.4 ks and 9.8 s at 1 mHz are 680000 and 2000 times larger than that (5 ms) in a conventional EDLC [29], respectively. A larger duration from 0.1 s to a few hours is required for practical use.

A liquid-phase capacitor such as an aluminum electrolyte capacitor generates leakage current by a parallel or series resistance through dc, resulting in an apparent enhancement in the capacitance. To clarify the enhancement in the capacitance accompanied by the decrement in the frequency, we calculated the frequency-dependent dielectric loss, tan δ, and series and parallel resistances, *Rs* and *Re*. These results are shown in fig. 4(b). With decreasing frequency, tan δ shows one peak at approximately 0.24 Hz and subsequently decreases close to zero, whereas *Rs* and *Re* increase from approximately 140 and 30 kHz, respectively, saturate from 1 to 0.2 Hz, and subsequently increase rapidly. The reason for the 0.24 Hz peak is still unclear. These results impose severe constraints on the possibility that the capacitance enhancement in the series and parallel circuits is caused by the leakage current of the capacitor in the low-frequency regions. Although the dielectric loss of 16.3 at 1 mHz is large, the dc capacitance can be increased considerably.

Finally, we consider the origin of the high-capacitance ATO. Figure 5(a) shows an equivalent circuit with two semicircles corresponding to the Nyquist diagram in fig. 3(a). Because the ATO with oxygen vacancies is characterized by electronic conduction [9,10], the equivalent circuit corresponding to the oblate semicircle can be recognized by a parallel circuit comprising an electric transport resistance, *Re*, and the electric double-layer capacitance, C_{dl}, at the uneven surface between the solid film and air [24]. Here, it should be noted that Pardo and Pickett showed that multilayer $(TiO_2)_5/(VO_2)_m$ nanostructures that have d^0/d^1 interfaces with no polar discontinuity revealed novel electronic states such as a metallic nature for $m \geq 5$ [30]. Hence, by analogy, we infer that the large numbers of TiO_2/VO_2 nanostructural interfaces in the upper layer become an electronic conduction state, leading to electrostatic induction of positive large charge to the uneven oxide surface. Figure 5(b) shows a schematic of a possible mechanism for the large electrical charges observed at the microscopic level. In an uneven surface with nanometer-sized cavities of ATO, electric double layers are formed at the electrically negative concave portion/air interfaces. This is the EDCC for ac applications. However, the AAO is characterized as a dc supercapacitor [8,10]. These results indicate the potential for further advances in the fabrication of amorphous titanium dioxide supercapacitors by enhancing a specific surface and integrating oxide ribbons in a nano-electromechanical system (NEMS).

* * *

We would like to thank Editage (`www.editage.com`) for the English language editing.

REFERENCES

[1] Winter M. and Brodd R. J., *Chem. Rev.*, **104** (2004) 4245.
[2] Whittingham M., *MRS Bull.*, **33** (2008) 411.
[3] Conway B. E., *Electrochemical Supercapacitors: Scientific Fundamentals and Technological Applications* (Plenum Press, New York) 1999.
[4] Simon P. and Gogotsi Y., *Nat. Mater.*, **7** (2008) 845.
[5] Aricó A. S., Bruce P., Scrosativ B., Tarascon J. M. and Schalkwijk W., *Nat. Mater.*, **4** (2005) 366.
[6] El-Kadyl M. F., Strong V., Dubin S. and Kaner R. B., *Science*, **335** (2012) 1326.
[7] Fukuhara M. and Sugawara K., *Nanoscale Res. Lett.*, **9** (2014) 253.
[8] Fukuhara M., Kuroda T., Hasegawa F. Hashida T., Kwon E. and Konno K., *EPL*, **123** (2018) 58004.
[9] Fukuhara M., in *Electronic Properties of Nanoclusters in Amorphous Materials* (Cambridge Scholars Publishing, Lady Stephen Library, Newcastle upon Tyne) 2019.
[10] Fukuhara M., Kuroda T. and Hasegawa F., *Sci. Rep.*, **6** (2016) 35870.

[11] Fukuhara M., Kuroda T., Hasegawa F., Shirai Y., Hashida T. and Konno K., *J. Alloys Compd.*, **776** (2019) 757.
[12] Fukuhara M. and Sugawara K., *Thin Solid Films*, **595** (2015) 1.
[13] Moh G. K., Varghese O. K., Paulose M., Shankar K. and Grimes C. A., *Sol. Energy Mater. Sol. Cells*, **90** (2006) 2011.
[14] Macak J. M. *et al.*, *Curr. Opin. Solid State Mater. Sci.*, **11** (2007) 3.
[15] Uchaker E., Zheng Y. Z., Li S., Candelaris S. L., Hu S. and Cao G. Z., *J. Mater. Chem. A*, **2** (2014) 18208.
[16] Musić S., Filipović-Vincekovic N. and Sekovanić L., *J. Chem. Eng.*, **28** (2011) 89.
[17] Kelley K. K., *The entropies of inorganic substances: Revision of data, Bulletin* (U.S. Bureau of Mines) 1950.
[18] Kubaschewski O. and Cartteral J. A., *Thermo-Dynamic Data of Alloys* (Pergamon, London) 1956.
[19] Inoue A. and Masumoto T., *Suppl. Sci. Rep. RITU A*, **March** (1980) 165.
[20] James P. F., *J. Mater. Sci.*, **10** (1975) 1802.
[21] Fukuhara M. *et al.*, *Phys. Status Solidi RRL*, **7** (2013) 447.
[22] Fukuhara M. *et al.*, *AIP Adv.*, **9** (2019) 095202.
[23] Wagner C. H., in *The NIST X-ray Photoelectron Spectroscopy (XPS) Database*, NIST Technical Note 1289 (NIST Publications) 1991.
[24] Itagaki M., in *Electrochemistry, Impedance Method*, 2nd edition (Maruzen, Tokyo) 2014, p. 93.
[25] Kötz R. and Carlen M., *Electrochim. Acta.*, **45** (2000) 2483.
[26] Conway B. E. and Pell W. G., *J. Power Sources*, **105** (2002) 169.
[27] Itagaki M., in *Electrochemistry, Impedance Method*, 2nd edition (Maruzen, Tokyo) 2014, p. 155.
[28] Ono S., Machida K., Asho H., Hashimoto H. and Fukuhara M., in *The 10th Porous Semiconductors-Science and Technology (PSST2016) Conference, Tarragona, Spain, 2015*, *Nanoscale Research Letters*, pp. 214–215.
[29] Okamura M., in *Electric Double Layer Capacitor and Its Storage System* (Nikkan Kogyo, Tokyo) 2011.
[30] Muraoka Y. *et al.*, *J. Appl. Phys.*, **109** (2011) 043702.